CHAPTER 7:

NICMOS Detectors

In this chapter...

7.1 Detector basics

In this section we briefly describe the operational principles of the NICMOS3 detectors. Figure 7.1 (adapted from McLean 1997) shows the basic physical structure of a photovoltaic HgCdTe detector.

Figure 7.1: Cross-section of a NICMOS3-type detector (not to scale).

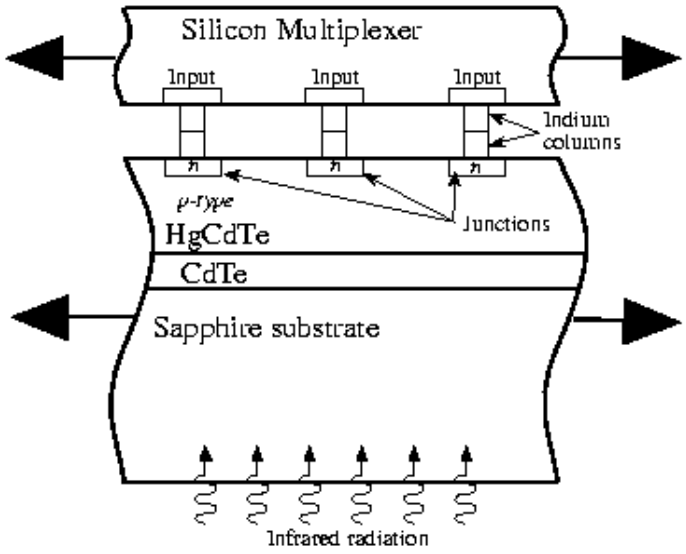

An infrared detector is basically a photodiode, the core of which is a p-n-junction created during the wafer processing. The Fermi-levels of the p- and n-type materials, i.e. the highest occupied energy state of the

electron gas within the semiconductor material, must match, which effectively creates an electric field across the junction. The incident infrared photons free electron-hole pairs into the conductance band at or near the junction which are immediately separated by the electric field. The accumulated charge carriers cause a voltage change across the junction which can be detected and used as a measure of the incident light. One can think of the detector as a capacitor that is discharged by the infrared photons. In practice, the voltage change is monitored by a Si field effect transistor (FET), used as a source follower amplifier. Figure 7.2 shows the equivalent circuit diagram for the NICMOS3 "unit cell".

Figure 7.2: Equivalent circuit diagram of the NICMOS3 unit cell.

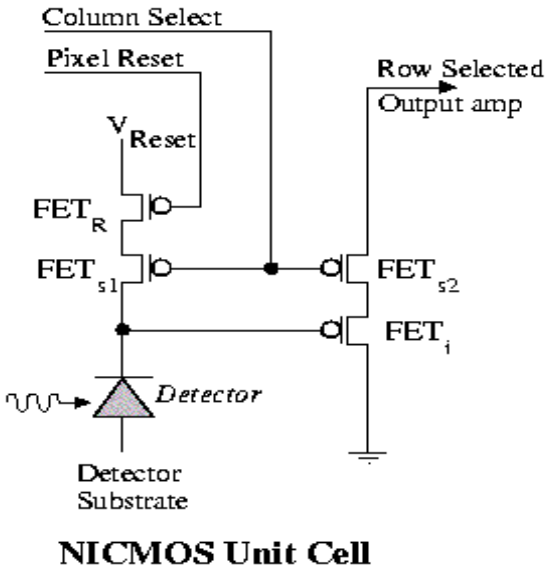

In order to produce an "imaging" detector, a large number of such unit cells, or pixels, are combined into an array. The photon-sensitive layer (HgCdTe in the case of NICMOS3 detectors) and the Si-multiplexer (which contains the array of FETs) are combined in a "hybrid" structure, connected via tiny indium bumps (Figure 7.3). For better mechanical stability, the "hybrid" array structure is put on an infrared-transparent Sapphire substrate. Since each pixel contains its own FET, there is no "bleeding" along columns, as in CCD chips, and bad pixels do not block the rest of the column.

Figure 7.3: Basic “hybrid” structure of infrared array detectors. Top: schematic of the detector array. Bottom: enlarged cross-section of a few unit cells, or pixels.

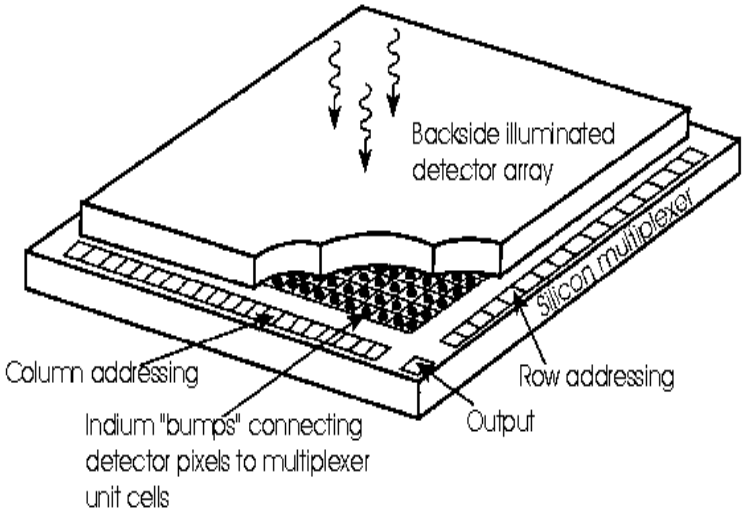

7.2 Detector Characteristics

7.2.1 Overview

Each NICMOS detector comprises 256 × 256 square pixels, divided into 4 quadrants of 128 × 128 pixels, each of which is read out independently. The basic performance of the nominal flight detectors is summarized in Table 7.1. Typically, the read-noise is ~27 e^-/pixel. Only a few tens of bad pixels (i.e., with very low response) were expected, but particulates—most likely specks of black paint, see Section 7.3.6—have increased this number to >100 per detector. The gain, ~5–6 e^-/ADU, has been set to map the full dynamic range of the detectors into the 16-bit precision used for the output science images.

Table 7.1: Flight Array Characteristics. Please see the following sections, which provide more information for each of the quantities listed.

Characteristics	Camera 1	Camera 2	Camera 3
Dark Current (e^- /second)[a]	0.3	0.3	0.3
Read Noise (e^-)[b]	~26	~26	~29
Bad Pixels (including particles)	213 (0.33%)	160(0.24%)	139(0.21%)
Conversion Gain (e^- / ADU)	5.4	5.4	6.5
Well Depth (ADU)	26,900	28,200	32,800
Saturation (ADU)[c] (95% Linearity)	21,500	22,500	26,200

Table 7.1: Flight Array Characteristics. Please see the following sections, which provide more information for each of the quantities listed.

Characteristics	Camera 1	Camera 2	Camera 3
50% DQE Cutoff Wavelength (microns)	2.55	2.53	2.52

a. These numbers are the typical signal level in a “dark” exposure, and can be used for sensitivity calculations. They contain contributions from linear dark current, amplifier glow, and possibly low-level cosmic ray persistence.
b. The quoted readout noise is the RMS uncertainty in the signal of a differenced pair of readouts (measured as the mode of the pixel distribution).
c. Saturation is defined as a 5% deviation from an (idealized) linear response curve.

7.2.2 Dark Current

A NICMOS exposure taken with the blank filter in place should give a measure of the detector dark current. However, the signal in such an exposure consists of a number of different components, such as linear dark current, amplifier glow, shading residuals, and possibly low-level cosmic ray persistence. The linear dark current is the signal produced by the minority carriers inside the detector material. It increases linearly with exposure time, hence the name. It can be measured after subtraction of amplifier glow and correction for shading (both of which we will describe below), avoiding exposures that are heavily impacted by cosmic ray persistence. The NICMOS calibration program has shown that the dark current levels of all three NICMOS cameras are stable and fully consistent with expectations for an operating temperature of ~77 K. This is demonstrated in Figure 7.4, which shows the results of the dark current monitoring program since the installation of the NCS.

Figure 7.4: Results from the NICMOS dark current monitoring program following the installation of the NCS. Shown are the monthly (bi-monthly since January 2003) linear dark current measurements for all three NICMOS cameras. Note that the linear dark current is stable within the measurement errors (a typical error bar for Camera 3 is shown in the upper left corner, the other cameras have errors about half of this).

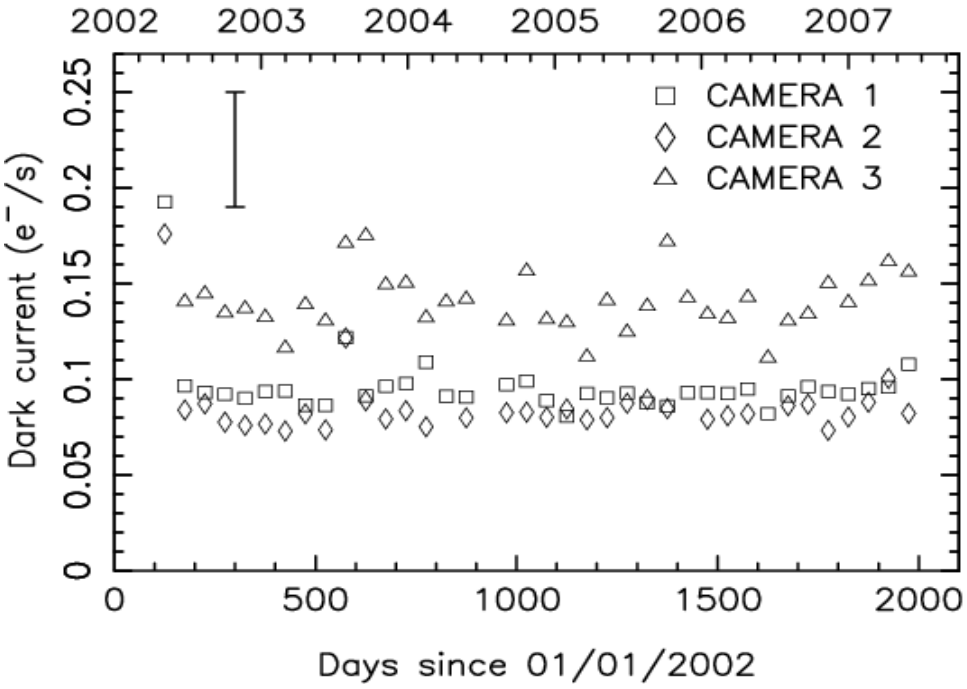

7.2.3 Flat Fields and the DQE

Uniformly illuminated frames—so-called “flat fields”—taken with the NICMOS arrays show response variations on both large and small scales. They also appear to change slightly as a function of time. These fluctuations are due to differences in the (temperature-dependent) Detector Quantum Efficiency (DQE) of the individual pixels. These spatial variations can be corrected in the normal way by flat fielding, which is an essential part of the calibration pipeline. Monitoring of the NICMOS flat-fields since the beginning of the NCS era in 2002, have shown a gradual change in the NICMOS DQE in both average response and spatial structure. These changes amount to between 1% and 3% on average. To correct for the small spatial variations, the NICMOS team has created a set of time dependent flat-fields (NICMOS ISR 2007-002). These flat-fields together with instructions are available at:

http://www.stsci.edu/hst/nicmos/calibration/reffiles/temporal_flat_files/index.html.

Figure 7.5 compares some of the current flat field exposures to those used in Cycle 7/7N. As can be seen both from the morphology of the images and the histograms of pixel values, the amplitude of DQE variations of all three cameras is much reduced at 77.1 K, thus making the response function “flatter”. This behavior is explained by the fact that “cold” pixels (i.e. pixels with a lower than average response) show a higher than average DQE increase with temperature.

Figure 7.5: Normalized pre- and post-NCS flat field responses for NIC1 (left) through NIC3 (right) for F110W, F187W, and F113N, respectively. The images are inverted to better display the grot; therefore, the dark regions have higher QE. The color stretch is the same for both temperatures in each camera. The histograms show the "flattening" of the arrays at the higher temperature (narrower distribution). The decrease in the dynamic range between bright and faint targets is a direct result of the decreased well depth at the higher temperature.

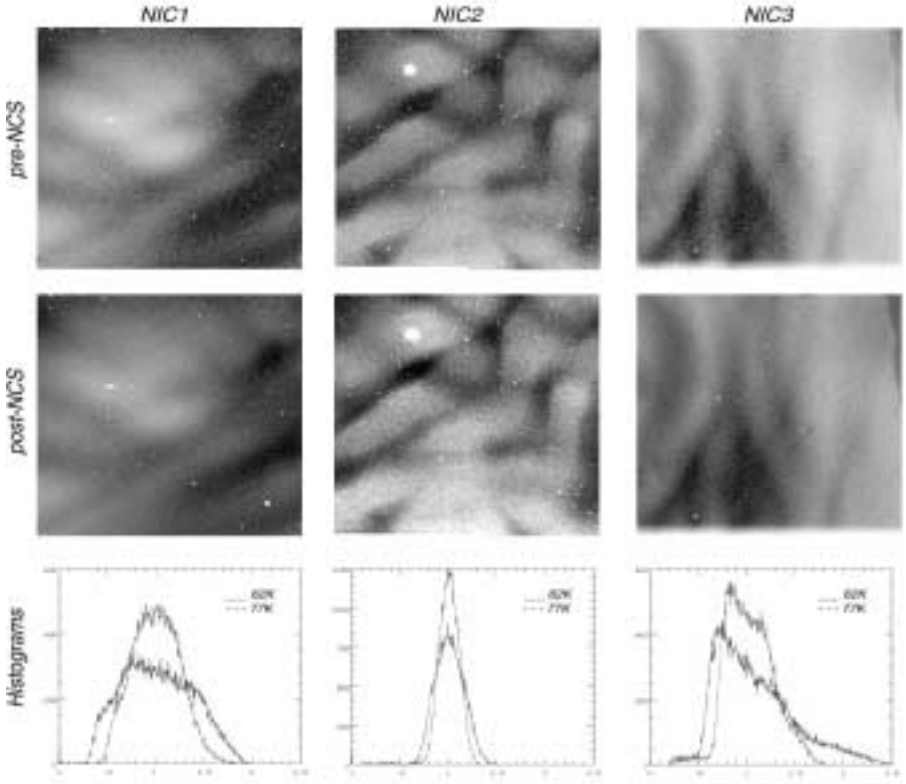

Flat field frames are generated from a pair of “lamp off” and “lamp on” exposures. Both are images of the (random) sky through a particular filter, but one contains the additional signal from a flat field calibration lamp. Differencing these two exposures then leaves the true flat field response. The count rate in such an image is a direct (albeit relative) measure of the DQE. The DQE increase of the three NICMOS cameras between 77.1 K and 62 K as a function of wavelength is presented in Figure 7.6.

Figure 7.6: NICMOS DQE: Comparison between post-SM3B (at operating temperature of 77K) and 1997/1998 (62K) eras.

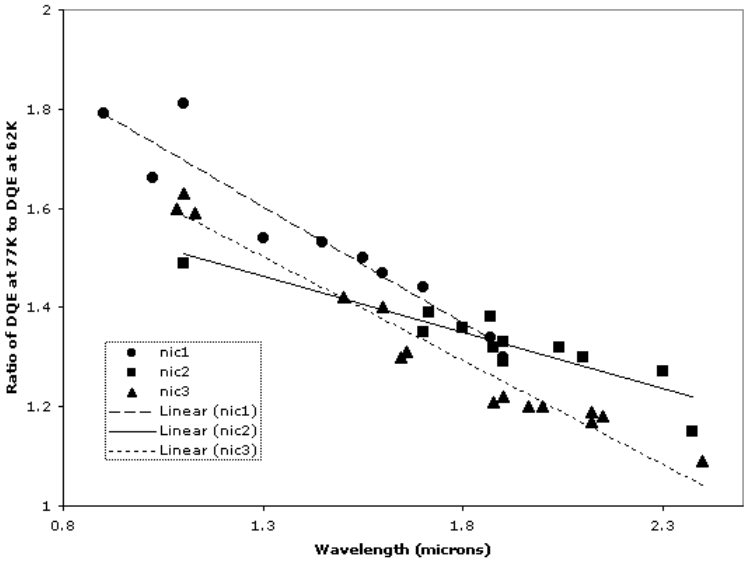

The average response at 77.1 K increased by about 60% at J, 40% at H, and 20% at K. The resulting wavelength dependence of the absolute DQE for NICMOS operations under the NCS is shown in Figure 7.7. Here, we have scaled the pre-launch DQE curve, which was derived from ground testing of the detectors, to reflect the changes measured at the wavelengths of the NICMOS filters. These (somewhat indirect) results have been confirmed by results from the photometric calibration program which uses observations of standard stars to measure the absolute DQE of NICMOS. The fine details in these DQE curves should not be interpreted as detector features, as they may be artifacts introduced by the ground-testing set-up. At the blue end, near 0.9 microns, the DQE at 77.1 K is ~20%; it rises quasi-linearly up to a peak DQE of ~90% at 2.4 microns. At longer wavelengths, it rapidly decreases to zero at 2.6 microns. The NICMOS arrays are blind to longer wavelength emission. When looking at the DQE curve, the reader should bear in mind that this is not the only criterion to be used in determining sensitivity in the near-IR. For example, thermal emission from the telescope starts to be an issue beyond ~1.7 μm. The shot-noise on this bright background may degrade the signal-to-noise obtained at long wavelengths, negating the advantage offered by the increased DQE.

It is important to note, especially for observations of very faint targets for which the expected signal-to-noise is low, that the DQE presented here is only the average for the entire array. Despite the flattening discussed above, the flat field response is rather non-uniform, and thus the DQE curves for individual pixels may differ substantially.

Figure 7.7: Relative increase of the NICMOS DQE as a function of wavelength for operations at 77.1 K, compared to pre-NCS operations at 62 K.

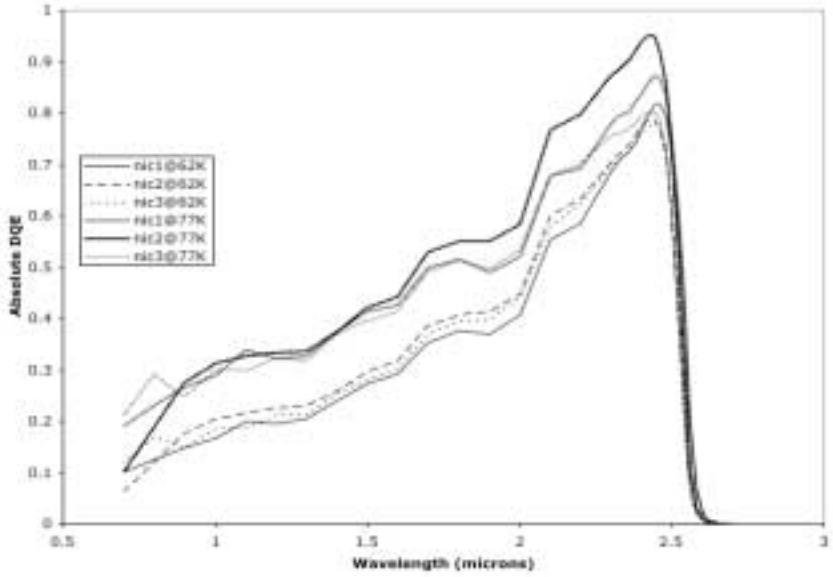

7.2.4 Read Noise

Each detector has four independent readout amplifiers, each of which reads a 128×128 quadrant. The four amplifiers of each detector generate very similar amounts of read noise. This is illustrated in Figure 7.8, which compares the pixel read noise distributions for the four quadrants of each NICMOS camera. The distributions for all quadrants are relatively narrow, with a FWHM of about 8 electrons, indicating that there are only few anomalously noisy pixels. The read noise is independent of temperature.

For some scientific programs such as ultra-low background observations (e.g. during the HDF campaigns), read noise can become a non-negligible component of the noise floor. The NICMOS group at STScI therefore has explored a method to lower the read noise in NICMOS data by reducing the digitization noise associated with the conversion from electrons to data numbers (DN). This can, in principle, be achieved by using a different conversion factor (i.e. gain) from e- to DN. Under optimal circumstances, this can produce a read noise reduction of 10–15%, resulting in exposures that reach up to 0.1 mag deeper. For details, we refer to Xu & Boeker (2003; NICMOS ISR-2003-006). However, the use of alternate gain settings requires calibration reference files (e.g. flat field or dark exposures) that have been obtained with the same gain. These files will not be obtained during the NICMOS calibration program. In addition, the CALNICA pipeline is currently not able to process such data correctly. Given the large operational overhead and the rather small scientific benefit, we strongly discourage NICMOS users from requesting non-standard gain settings. In exceptional circumstances, such requests will be considered on a

case-by-case basis with the understanding that proper calibration of such data is the sole responsibility of the GO.

Figure 7.8: Read noise characteristics of the three NICMOS detectors. Each panel shows the pixel distribution of electronics-induced RMS uncertainties, as measured from a series of difference images of short (0.2s) DARK exposures.

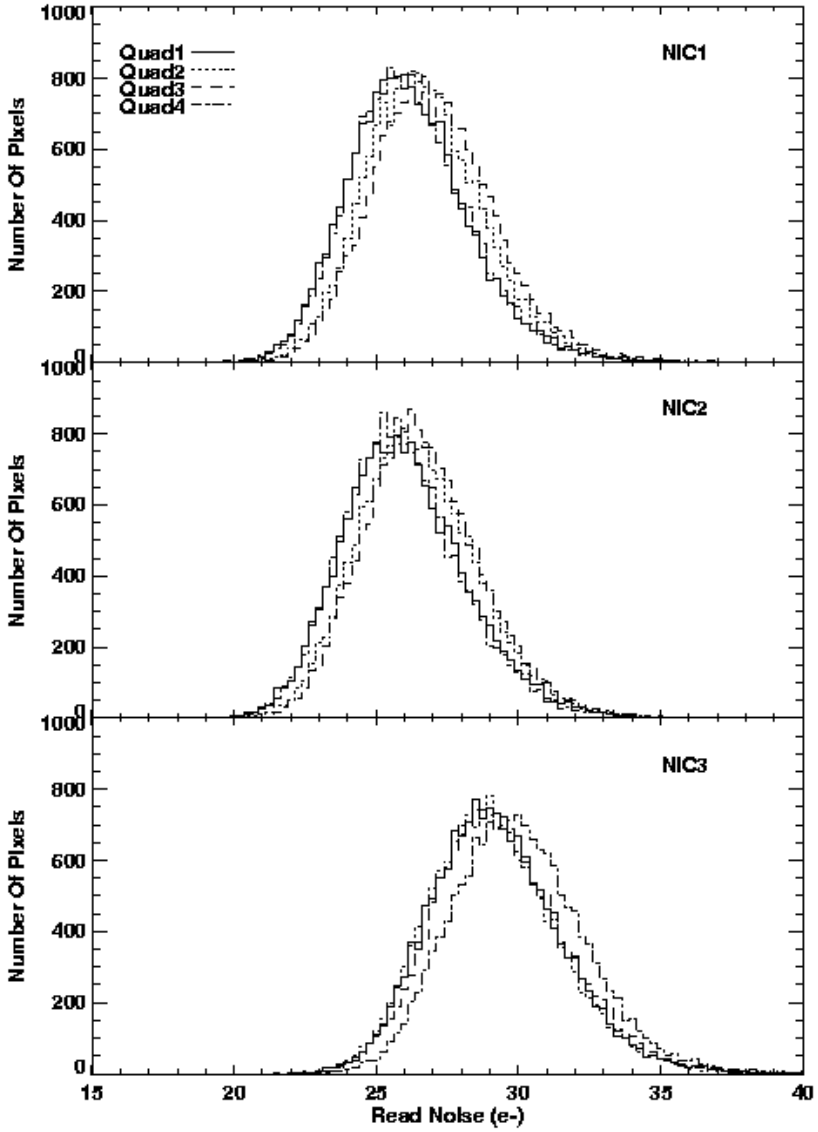

7.2.5 Linearity and Saturation

Throughout Cycle 7, the linearity correction of the calibration pipeline had been based on the assumption that the NICMOS detector response was well approximated by a linear function until pixel counts reached a certain threshold. Therefore, no linearity correction was performed below this

point. However, the ongoing NICMOS calibration program has shown that the detector response is in fact (slightly) non-linear over the full dynamic range. Figure 7.9 illustrates this behavior.

Figure 7.9: Count rate as a function of total accumulated counts for a typical NICMOS detector pixel. Note that the pixel response is non-linear (i.e., the count rate is not constant) over the entire dynamic range.

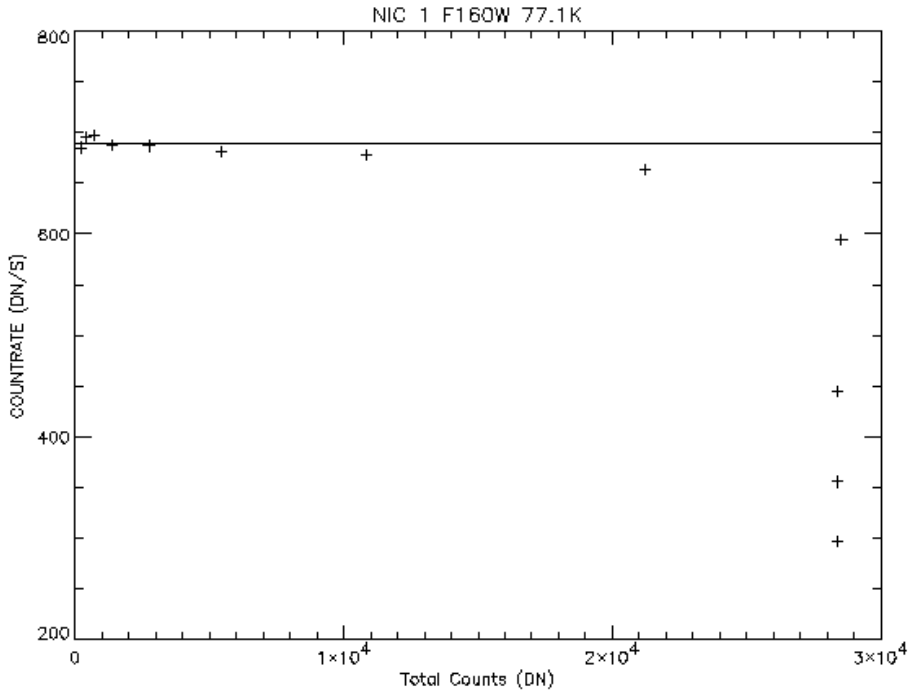

A revised linearity correction was therefore implemented in the NICMOS calibration pipeline (Cycle 11 and beyond), which corrects data over the entire dynamic range between zero and the flux level at which the response function deviates by more than 5% from the linear approximation. Pixels that reach this threshold during an exposure are flagged as saturated, and are not corrected during the pipeline processing. This saturation point typically occurs at about 80% of the well depth.

7.2.6 Count Rate Non-Linearity

NICMOS has a significant count rate dependent non-linearity that also depends on wavelength as described in Section 4.2.4. While we have no physical explanation for the effect at the time of this writing, we currently assume it arises in the detector. Objects fainter than the NICMOS standard stars of about the 12th magnitude will be measured too faint, objects that are brighter than our standards will seem too bright. The maximum offsets on dark sky backgrounds at F110W are about 0.25 mag in NIC1 and NIC2, and about 0.16 mag in NIC3. Software has been developed to linearize the

counts in imaging observations. More details on the effect and how to correct for it can be found at:

http://www.stsci.edu/hst/nicmos/performance/anomalies/nonlinearity.html.

7.3 Detector Artifacts

7.3.1 Shading

The NICMOS arrays exhibit a noiseless signal gradient orthogonal to the direction of primary clocking, which is commonly referred to as *shading*. It is caused by changes of the pixel bias levels as a function of temperature and time since the last readout ("delta-time"). The amplitude of the shading can be as large as several hundred electrons for some pixels under some circumstances. The first pixels to be read show the largest bias changes, with the overall shading pattern decreasing roughly exponentially with row number. The shading is a noiseless contribution to the overall signal, therefore it can be completely removed during pipeline processing once it has been calibrated with delta-time and temperature.

For a given delta-time (and temperature), the bias level introduced by the shading remains constant. For `MULTIACCUM` readout sequences (see Chapter 8) where the time between readouts is increasing logarithmically, the bias level changes with each successive read, and thus the overall shading pattern evolves along the `MULTIACCUM` sequence. We have calibrated the dependence of shading as a function of delta-time for each of the three NICMOS detectors. This information is used by the **calnica** pipeline to construct synthetic dark current reference files for NICMOS observations. The accuracy of this calibration is good (a few percent for most readout times).

The 1999 warm-up monitoring program has shown that the shading signal is temperature dependent. Nevertheless, the good temperature-stability of the NICMOS/NCS system has enabled accurate shading correction of NICMOS data with a single set of dark current reference files. Figure 7.10 presents the shading profiles for each camera at the operating temperature of 77.1 K.

The NICMOS group at STScI will continuously monitor both shading behavior and NICMOS temperature stability, and will provide additional calibration files should this become necessary.

Figure 7.10: Shading profiles for all camera/delta-time combinations measured at 77.1 K (NCS era). The profiles were created by collapsing a dark exposure of the respective integration time along the fast readout direction (after correction for linear dark current and amplifier glow).

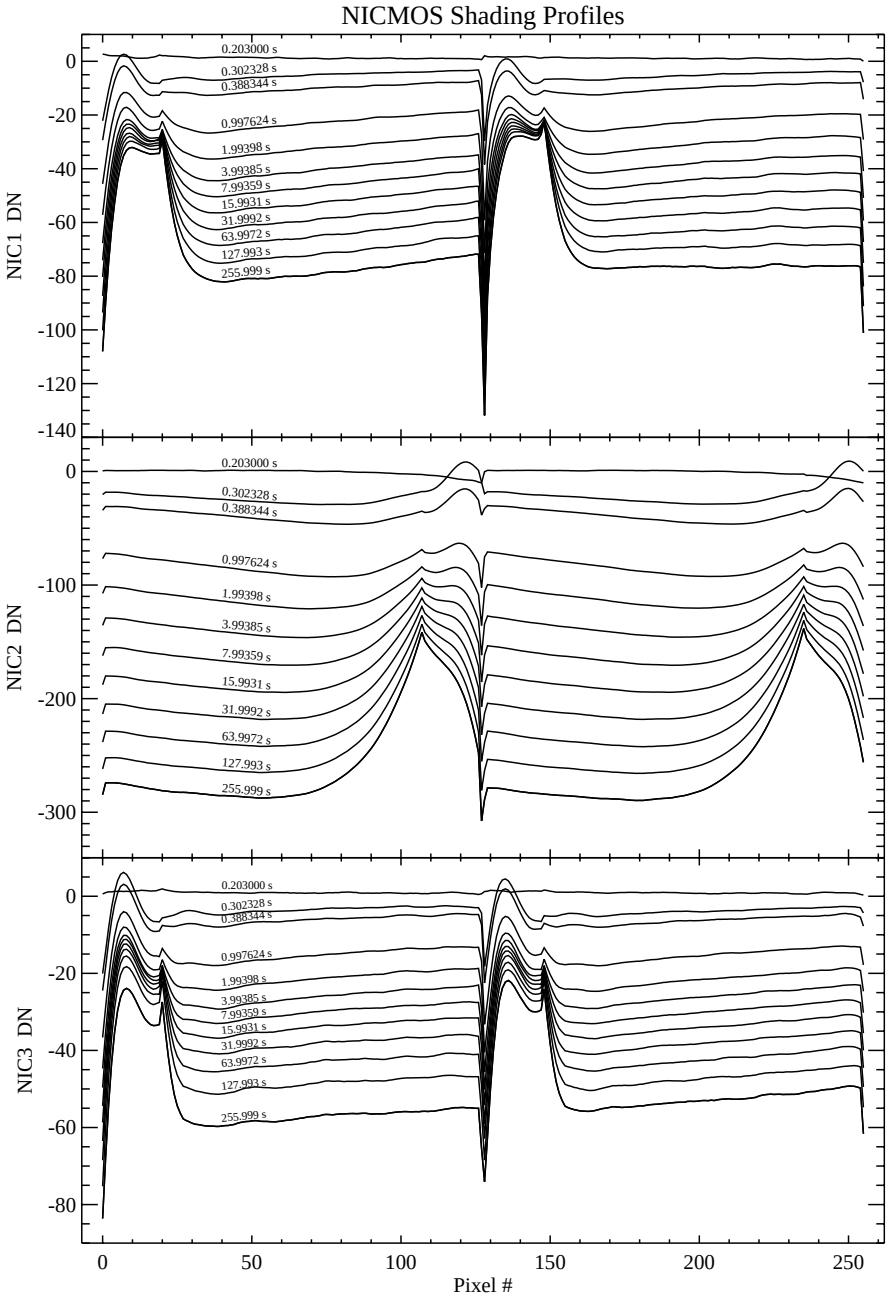

7.3.2 Amplifier Glow

Each quadrant of a NICMOS detector has its own readout amplifier situated close to the corners of the detector. Each time the detector is read out, the amplifier warms up and emits infrared radiation that is detected by the chip. This signal, known as amplifier glow, is largest in the array corners with ~80 e^-/read, and falls rapidly towards the center of the detector where it is about 10 e^-/read. The signal is cumulative with each non-destructive readout of an exposure. It is highly repeatable, and is exactly linearly dependent on number of reads. It also is constant with temperature, as shown in Figure 7.11.

Figure 7.11: Amplifier glow signal as a function of detector temperature.

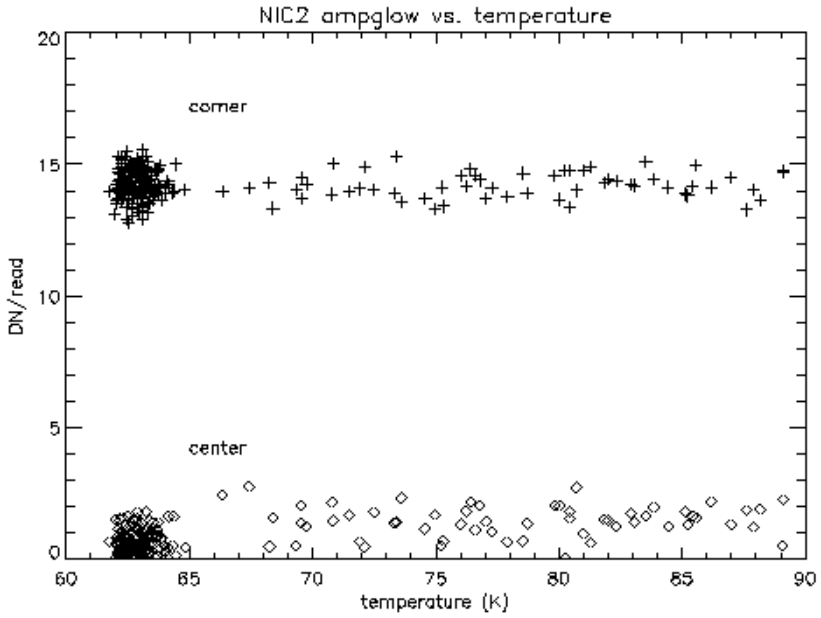

In contrast to the shading, the amplifier glow is a photon signal, and thus is subject to Poisson statistics. It therefore contributes to the total noise in NICMOS exposures. Amp-glow images for all three cameras are shown in Figure 7.12. In case of an ACCUM exposure with multiple initial and final reads (see Chapter 8), the photon noise produced by amplifier glow can outweigh the read noise reduction from the multiple reads, especially close to the array corners producing a total noise reduction never larger than ~40 –50%. Similarly, the trade-off between improved cosmic ray rejection, reduced read noise, and increased photon noise in a MULTIACCUM sequence is complicated.

Figure 7.12: Amplifier glow for Cameras 1 (left) through 3 (right), on a uniform grayscale, and below a plot of rows (near the bottom) of each camera.

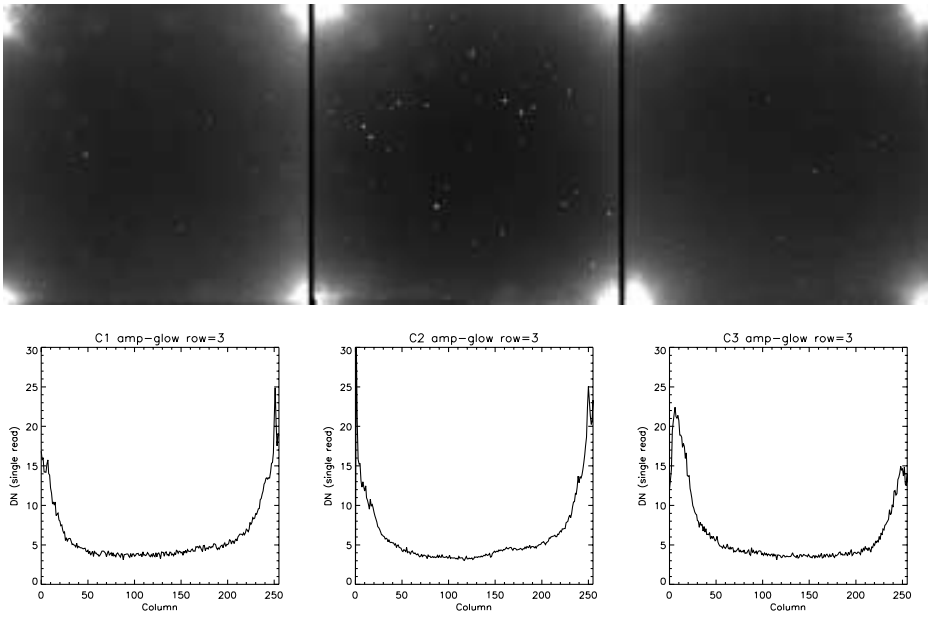

7.3.3 Overexposure of NICMOS Detectors (XXX Update this Section XXX)

Effects of photon and cosmic-ray persistence are described in Section 4.6.

7.3.4 Electronic Bars and Bands

Electronic ‘‘bars’’ are an anomaly in NICMOS data taken during Cycles 7 and 7N. They appear as narrow stripes that cross the quadrants of an array, and occur identically in all 4 quadrants at the same rows/columns in each. The bars are caused by pick-up of an amplifier signal on one of the row/column address lines, causing a momentary change in the bias for that pixel.

Similarly, electronic ‘‘bands’’ are caused when one of the NICMOS detectors is reset while another is being read out. The reset pulse causes a sudden jump in the bias of the detector which is being read. The bias jump then appears as an imprint on the image that looks like a band.

The bars typically run the length of a quadrant (128 pixels), and are 3 pixels wide—the first pixel is lower than the mean, the second is at the mean level and the third is higher than the mean, giving the impression of an undersampled sinusoidal spike with an amplitude of up to ~10 DN peak-to-peak. If a bar appears in the 0th readout, it will be subtracted from all the other readouts as part of the normal calibration process, and will

appear to be a negative of the above description. The bars run parallel to the slow readout direction, which is vertical in NIC1, and horizontal in NIC2 and NIC3. They are almost always broken in at least one place, with a shift of 2–10 pixels in the narrow direction. A more detailed description of the electronic bars and bands is given on the NICMOS WWW site:

http://www.stsci.edu/hst/nicmos.

In Cycle 11, we implemented a modified readout sequence for the three NICMOS cameras which reduces the probability that a detector will be reset while another is being read. This procedure is completely transparent to users and has significantly reduced the electronic bands problem.

7.3.5 Detector Cosmetics (XXX Update this Table? XXX)

Each NICMOS detector has a number of pixels that show an anomalous responsivity. Such “bad pixels” come in various flavors. So-called “hot” pixels have a higher than average dark current, and thus show excessive charge compared to the surrounding pixels. On the other hand, “cold pixels” are less sensitive to incident photons than the typical pixel. The anomalously low responsivity of a “cold” pixel could be due to either a lower intrinsic DQE of the pixel, or due to grot (see below). Some pixels do not even respond at all (“dead pixels”) to incoming light. Quantitative statistics of the hot/cold pixels in the three NICMOS cameras are given in Table 7.2. It is important to note that the impact of bad pixels on the quality of NICMOS images can be minimized by dithering the observations.

Table 7.2: Bad Pixels in NICMOS

Pixel Characteristics	NIC1	NIC2	NIC3
Cold[a]	467	480	541
Hot[b]	1359	1429	1859

a. Numbers include pixels affected by grot (see Section 7.3.6). A cold pixel is defined as having a response 5 sigma lower than the median value of all pixels.
b. A hot pixel is defined as having more than three times the median dark current of the array.

7.3.6 "Grot"

On-orbit flat field exposures taken after the NICMOS installation in 1997 revealed a population of pixels with very low count rates that had not previously been seen in ground testing. It is believed that these pixels are at least partly obscured by debris on the detector surface, most likely small

paint flakes that were scraped off one of the optical baffles during the mechanical deformation of the NICMOS dewar. Additional grot has collected on the detectors since its revival. NIC1 appears to be the most affected with an additional chunk of grot in the lower right quadrant. This so-called “grot” affects approximately 100–200 pixels in each NICMOS camera. The largest pieces of grot in NIC1 are shown in Figure 7.13. Again, dithering is recommended to minimize the impact of grot.

Figure 7.13: A NIC1 flat field image shows the largest of the groups of pixels affected by debris (“grot”). These bits of “grot” are roughly 5 by 9 pixels (upper left) and 5 by 6 pixels (lower right).